

#### Contents lists available at ScienceDirect

#### Materialia

journal homepage: www.elsevier.com/locate/mtla



Full Length Article

## Microstructure design and *in-situ* investigation of TRIP/TWIP effects in a forged dual-phase Ti–10V–2Fe–3Al alloy



Y. Danard<sup>a</sup>, R. Poulain<sup>a</sup>, M. Garcia<sup>a</sup>, R. Guillou<sup>b</sup>, D. Thiaudière<sup>c</sup>, S. Mantri<sup>d</sup>, R. Banerjee<sup>d</sup>, F. Sun<sup>a</sup>, F. Prima<sup>a,\*</sup>

- <sup>a</sup> PSL Research University, Chimie ParisTech, Institut de Recherche de Chimie Paris, CNRS UMR 8247, 75005 Paris, France
- <sup>b</sup> DEN-Service de Recherches Métallurgiques Appliquées (SRMA), CEA, Université Paris-Saclay, F-91191 Gif-sur-Yvette, France
- <sup>c</sup> Synchrotron SOLEIL, l'orme des merisiers, Saint-Aubin BP48, F-91192 Gif-sur-Yvette, France
- $^{
  m d}$  Department of Materials Science and Engineering, University of North Texas, Denton, TX 76207, USA

#### ARTICLE INFO

# Keywords: Titanium alloys Ti-10V-2Fe-3Al forged microstructures TRIP/TWIP effects heterogeneous deformation in-situ investigation

#### ABSTRACT

Strain-transformable Ti-based alloys are known to display a superior combination of strength, ductility and strain-hardening and attracted considerable interest on recent years. They generally still display, however, a limited yield strength that can be possibly overcome by further precipitation strengthening of the developed systems. In that work, we developed a design strategy to reach a forged dual-phase  $(\alpha+\beta)$  microstructure with TRIP/TWIP properties in a Ti–10V–2Fe–3Al alloy. The results showed an excellent combination of mechanical properties due to the strain-transformable deformed  $\beta$ -matrix. The investigation on the deformation mechanisms in the Ti–10V–2Fe–3Al alloy was accurately performed by means of both *in-situ* synchrotron XRD, mechanical testing followed ySEM/EBSD mapping and "post mortem" TEM microstructural analyses. Combined Twinning Induced Plasticity (TWIP) and Transformation Induced Plasticity (TRIP) effects were shown to be intensively activated in the alloy. The particular role of stain-induced martensite  $\alpha''$ , acting as a relaxation mechanism at the  $\alpha/\beta$  interfaces, as well as the strong interactions between mechanical twins and primary  $\alpha$  nodules were particularly highlighted.

#### 1. Introduction

In recent years, a new family of metastable  $\beta$  titanium alloys displaying a superior combination of strength, ductility and enhanced strainhardenability has been extensively investigated. These alloys combine TRansformation Induced Plasticity (TRIP) and TWinning Induced Plasticity (TWIP) effects resulting in both complex deformed microstructures and extremely efficient dynamical strain-hardening mechanisms (dynamical Hall-Petch, mechanical contrast between twins and matrix due to the high elastic anisotropy of  $\beta$ -phase, hetero-deformation induced strain-hardening) [1-7]. Most of the alloys developed to date have been based on a "d-electron" design approach for single  $\beta$  phase microstructures [8]. These alloys typically exhibit low yield strengths and therefore enhancing the yield strength while preserving large tensile ductility and strain hardenability remains a challenge. For that purpose, additional precipitation strengthening approaches have been already successfully proposed, for example  $\omega$  phase precipitation [9]. However, there is still limited information related to TRIP/TWIP effects in conventionally strengthened  $\alpha+\beta$  dual-phase microstructures [10]. Yield strength improvement can be, however, expected from that approach, considering

\* Corresponding author.

E-mail address: frederic.prima@chimieparistech.psl.eu (F. Prima).

that  $\alpha$  particles may significantly decrease the observed mean-free path of the mechanical twins, for example. Several critical questions may arise from that strategy: (i) the  $\beta$  phase compositional design has to be performed considering both the nominal compositional design and the targeted  $\alpha$  phase volume fraction. (ii) The  $\alpha$  phase precipitation has to be ensured in a well-controlled manner with homogeneous distribution to avoid excessive stress-concentration. Considering these different facts, we propose in this paper a simplified and straightforward way to reach conventionally strengthened  $\alpha+\beta$  dual-phase with combined TRIP/TWIP properties and resulting in high strain-hardenability. For that purpose, an as-forged industrial Ti-10V-2Fe-3Al (wt%) has been used as starting material and a strain-transformable microstructure has been generated from a single and well controlled solution treatment. Advantages may be multiple: (1) Ti-10V-2Fe-3Al is a fully available commercial Ti alloy from the near- $\beta$  family. (2) It is already widely used as large structural parts in aerospace industry (landing gear). (3) Properties of Ti-10V-2Fe-3Al can be tailored over a very wide range, from superelasticity in the single  $\beta$  phase metastable state [11], to a high strength alloy when used in a classical bimodal microstructural state, composed of both primary  $(\alpha_n)$  and secondary  $(\alpha_s)$  alpha phase [12–14]. To establish the proof of concept, the microstructural design approach followed in this work is firstly presented. The investigation of resulting deformation mechanisms is mainly based on a combination of in-situ mechanical testing, coupled with synchrotron x-ray diffraction measurements (SXRD)

and electron backscatter diffraction (EBSD) studies in a scanning electron microscope (SEM), as a function of the strain. Finally, results of preliminary transmission electron microscopy (TEM) investigations of the interaction of mechanical twins with  $\alpha$  precipitates, after interrupted tensile tests, has been presented in this paper.

#### 2. Material and methods

Ti-10V-2Fe-3Al (in wt%) (Ti-1023) as-forged bars, with a  $\beta$  transus equal to 1073 K, had been provided by TIMET for this study. Samples with dimensions of  $55 \times 18 \times 10 \text{ mm}^3$  were solution-treated in the  $\alpha + \beta$ field at 1023 K for 14.4 ks and then water quenched. Tensile specimens with dog bone shape and gauge dimensions of  $55 \times 6 \times 3 \,\mathrm{mm}^3$  were machined. Tensile tests were performed at room temperature, at a strain rate of  $10^{-3}$  s<sup>-1</sup>, on a Criterion 43 MTS machine equipped with an extensometer with a gauge length of 25 mm. All specimen for both conventional x-ray diffraction (XRD) and synchrotron x-ray diffraction (SXRD) analyses were first prepared by mechanical polishing on SiC papers and using an OPS-H2O2-H2O mixture for final polishing. The surface of specimens for EBSD were prepared by electropolishing. Microstructures were observed using a field emission gun scanning electron microscope (FEG-SEM ZEISS LEO1530) operated at 20 kV. X-ray diffraction measurements were collected using a Bruker Endeavor D8 X-ray diffractometer. EBSD scans were collected under in-situ tensile conditions, with step size ranging from 0.03 to 0.5 µm, at the initial state, at 5% of deformation and then after unloading. In-situ tensile tests, both for synchrotron and SEM, were performed using a Proxima 100-Micromecha machine on  $55\,\text{mm} \times 1.5\,\text{mm} \times 1\,\text{mm}^3$  samples. In-situ SXRD scans were carried out at the DiffAbs (Diffraction and Absorption) beamline at SOLEIL, the French synchrotron facility. XRD measurements were performed in reflection mode with an energy of the X-ray beam fixed to 12.475 keV  $(\lambda=0.994 \,\text{Å})$ . Using this energy combined with an incident angle of 9°, the penetration depth was approximately 20  $\mu$ m. A  $600 \times 300 \,\mu$ m<sup>2</sup> x-ray beam size (HxV fwhm) at the center of the 6-circle diffractometer was used in order to obtain good statistics of grains during measurements. However, the average grain size in these samples had been measured to be around 300 µm. As a consequence, it can be estimated that no more than two or three grains were actually analysed. The diffraction patterns were recorded thanks to a bi-dimensional XPAD-S140 detector (hybrid pixel technology, 560×240 pixels<sup>2</sup> image size) [15],[16]. The detector was mounted on the  $2\theta$  goniometer arm with a detector sample distance of 580 mm (granting an angular resolution of 0.013°). After recording, each diffraction pattern was converted to diffraction diagram (radial integration) with a typical [37.3°-41°]  $2\theta$  angular range. TEM samples were prepared using twin-jet electropolishing technique. A JEOL 2100Plus transmission electron microscope (TEM) operating at 200 kV was used to carry out microstructural analyses.

#### 3. Results and discussion

#### 3.1. Design of a strain-transformable microstructure in Ti-10-2-3

The proposed strategy is related on a fine tuning of the initial microstructure to get a well-controlled  $(\alpha+\beta)$  dual-phase with a straintransformable  $\beta$  matrix phase. As stated earlier, the deformation behavior of the  $\beta$  phase is largely controlled by its chemical composition and stability/metastability [14],[17–19]. The  $\beta$  composition in turn requires controlling the chemical partition of alloying elements between  $\alpha$  and  $\beta$  phases, respectively, and therefore it becomes necessary to tune the  $\alpha$  phase volume fraction in Ti-10-2-3. Based on extensive previous work on TRIP/TWIP Ti alloys, the stability range for strain-transformable single-phase alloys has been evaluated to lie around the empirical stability parameter Mo<sub>eq</sub> =12 [1]. The  $\beta$  phase Mo<sub>eq</sub> value in case of Ti-10-2-3 has been clearly shown to evolve progressively as a function of  $\alpha$  phase volume fraction with an obtained value of 12 as Mo<sub>eq</sub> parameter for an  $\alpha$  phase volume fraction at 20% [12]. Therefore, in the present study,

the as-forged Ti-10-2-3 sample has been subjected to different annealing treatments between 1003 K and 1043 K, in the  $\alpha+\beta$  two-phase region. These annealing treatments have been optimized on the basis of  $\alpha$  volume fraction, and the final treatment that was selected was annealing at 1023 K ( $T_{\beta}$ – 50 K) for 14.4 ks.

#### 3.2. Initial microstructure and resulting mechanical properties

The initial microstructure is a typical as-forged microstructure as shown in Fig. 1(a). A bimodal distribution of  $\alpha$  phase can be observed, composed of both primary  $(\alpha_p)$  nodules and secondary  $(\alpha_s)$  laths. The average  $\beta$  grain size is of about 300  $\mu$ m, however it can be noticed that the  $\beta$  grains are fragmented into  $\beta$  sub-grains ranging from 5 to 10  $\mu$ m in size. This  $\beta$  grain fragmentation is produced, along with  $\alpha_{\rm p}$  globularization, during the last step of hot forging in the  $(\alpha+\beta)$  field [14],[17–19]. From this initial as-forged microstructure, a single step solution treatment at 1023 K for 14.4 ks is performed to dissolve the  $\alpha_s$  laths, to preserve a controlled volume fraction (20%) of homogeneously dispersed  $\alpha_{\rm p}$  nodules and to complete  $\alpha_{\rm p}$  nodules globularization. The resulting microstructure is presented in Fig. 1(b) and (c) and shows a dual phase microstructure composed of a fine and homogeneous dispersion of globularized  $\alpha_{\rm p}$  nodules of 3 µm in average size in the  $\beta$  matrix. It should be noted that the  $\alpha_p$  nodules are mainly located at the  $\beta$  sub-grains boundaries. As a consequence, it is likely that these  $\alpha_{\rm p}$  precipitates display a noticeable misorientation with respect to the Burgers Orientation Relationships (BOR) with, at least, one of the neighboring misoriented  $\beta$ sub-grains. The  $\alpha_{\rm p}$  volume fraction has been estimated to be 19% with the EBSD phase map (Fig. 1(c)).

The associated tensile stress-strain curve (Fig. 2, in red) displays a remarkable combination of mechanical properties with a good yield strength YS<sub>0.2</sub> = =670 MPa and a high ultimate tensile strength UTS=1120 MPa. The maximum uniform tensile strain is very high at 0.30 and is associated with an extremely stable strain-hardening rate showing a large plateau at 1400 MPa. In comparison the tensile stressstrain and work-hardening curves of the initial as-forged microstructure are given in black in the Fig. 2. These curves show a higher yield strength but very limited work-hardening capability and uniform deformation at fracture. The evolution of mechanical properties validates the design strategy: the precipitation of a controlled percentage of  $\alpha_p$  precipitates leads to a large improvement of the work-hardening rate and the tensile strain. It can also be noticed that, thanks to the better work-hardening capacity, the tensile strength is higher on the tensile curve of the Ti-1023 solution treated in the  $\alpha+\beta$  field compared to the as-forged state. This result is close to the targeted properties of this present work and is consistent with previous experimental results on alloys presenting combined TRIP and TWIP effects on loading [1-7],[20]. It is worth noting that the presently displayed mechanical properties are equal or even superior to most of the TRIP/TWIP alloys reported so far.

#### 3.3. In-situ observation of the associated deformation mechanisms

The main deformation mechanisms, and more particularly the strain-induced martensite formation, were first characterized, on loading, by *in-situ* SXRD. The obtained results are reported in Fig. 3(c), displaying the evolution of the SXRD diagrams as the strain is increased, up to 8% and then unloaded. It should be noted that the diffraction range has been selected specifically for strain-induced martensite precipitation and as a consequence, no  $\beta$  phase diffraction peak is visible in that range (Fig. 3(c)). However,  $\beta$  peaks are present in the whole-range diagrams (Fig. 3(a)). In the initial stage (0% strain), the diffractogram shows the presence of the  $\alpha_p$  phase ((11–20) diffraction) and no  $\alpha''$  martensite after the annealing treatment, consistently with the EBSD analyses (Fig. 1). At 2% strain, diffraction peaks corresponding to the (200) and the (130) planes of the strain-induced martensite  $\alpha''$  are observed to progressively grow on loading, confirming an early TRIP effect in the dual-phase Ti–10V–2Fe–3Al alloy, consistently with the observed

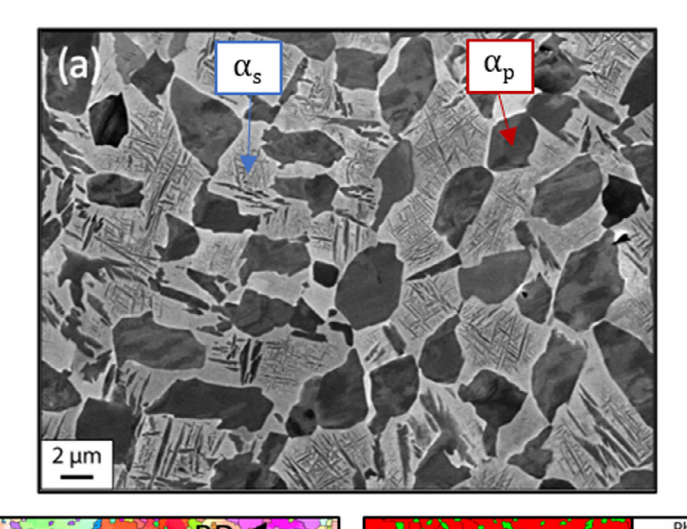


**Fig. 1.** (a) Backscatter electron image of the as-forged microstructure. EBSD mapping of the initial microstructure before deformation: (b) inverse pole figure (IPF) along the normal direction, and (c) corresponding phase map with  $\beta$  in red and  $\alpha$  in green. (For interpretation of the references to color in this figure legend, the reader is referred to the web version of this article.)

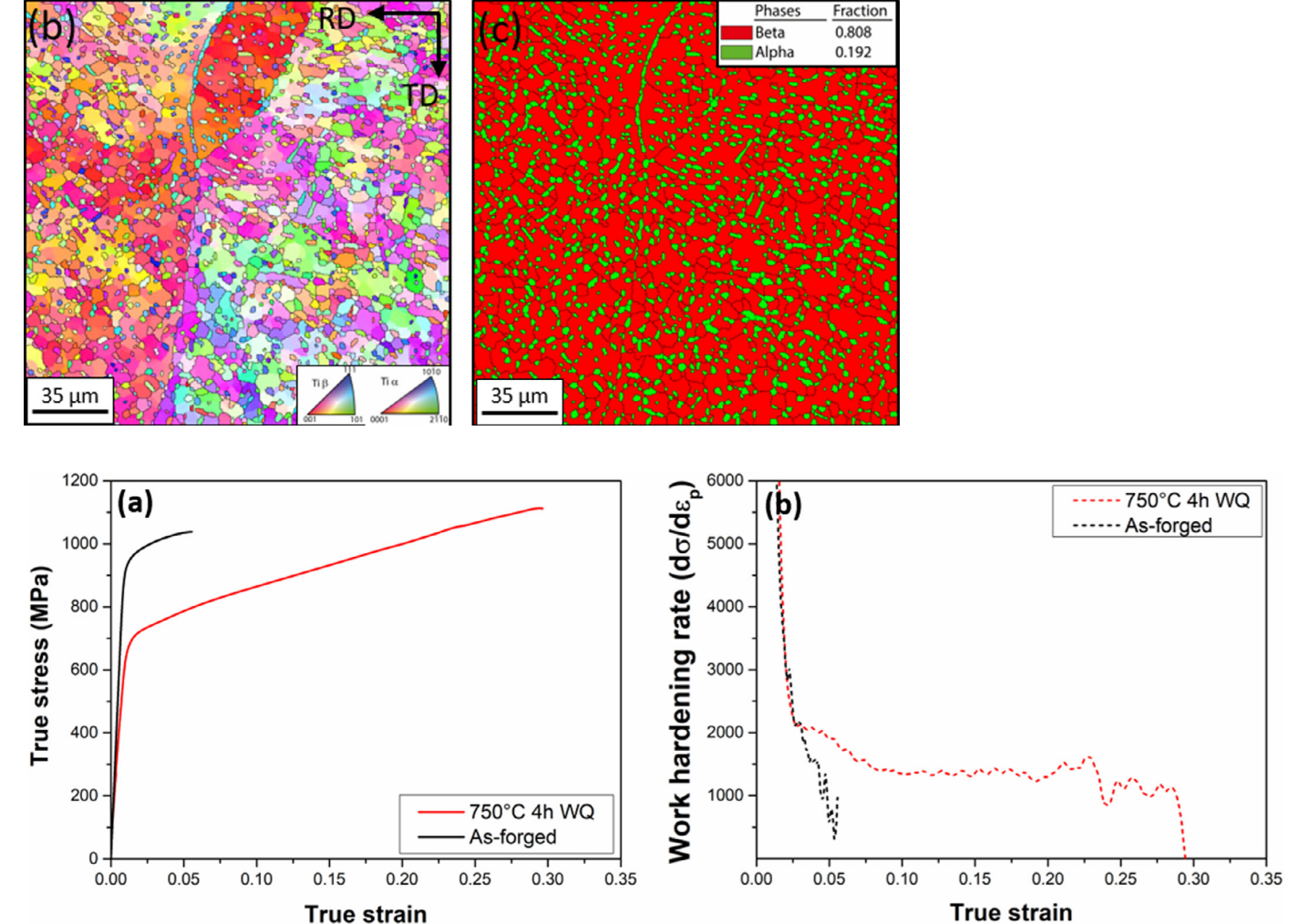


**Fig. 2.** (a) True stress-true strain and (b) work-hardening rate curves of Ti-10V-2Fe-3Al (wt%) alloy solution-treated in the  $\alpha+\beta$  field (in red) and as-forged (in black). (For interpretation of the references to color in this figure legend, the reader is referred to the web version of this article.)

mechanical properties where a slight bump is visible on the onset of the plastic range (Fig. 2). As the deformation increases, up to 8%, the intensity of the  $\alpha''$  peaks increases continuously, specifically referring to the (200)  $\alpha''$  peak. Two different facts look interesting in the set of diffractograms: (1) the strain-induced  $\alpha''$  martensite appears to be almost fully reversed after unloading from 8% strain, indicating a high degree of martensite reversibility in this alloy, even when compared to classical

superelastic alloys [21]. Intriguingly, it is worth noting that the complete reversion of the stress-induced martensite is presently not associated with any superelastic effect after a 8% strain (2) the  $(11-20)_{\alpha}$  peak shifts to higher angles during the deformation and then shows a tendency to shift back to its initial position during unloading which seems to indicate a large elastic deformation of the  $\alpha$  phase on the onset of loading.

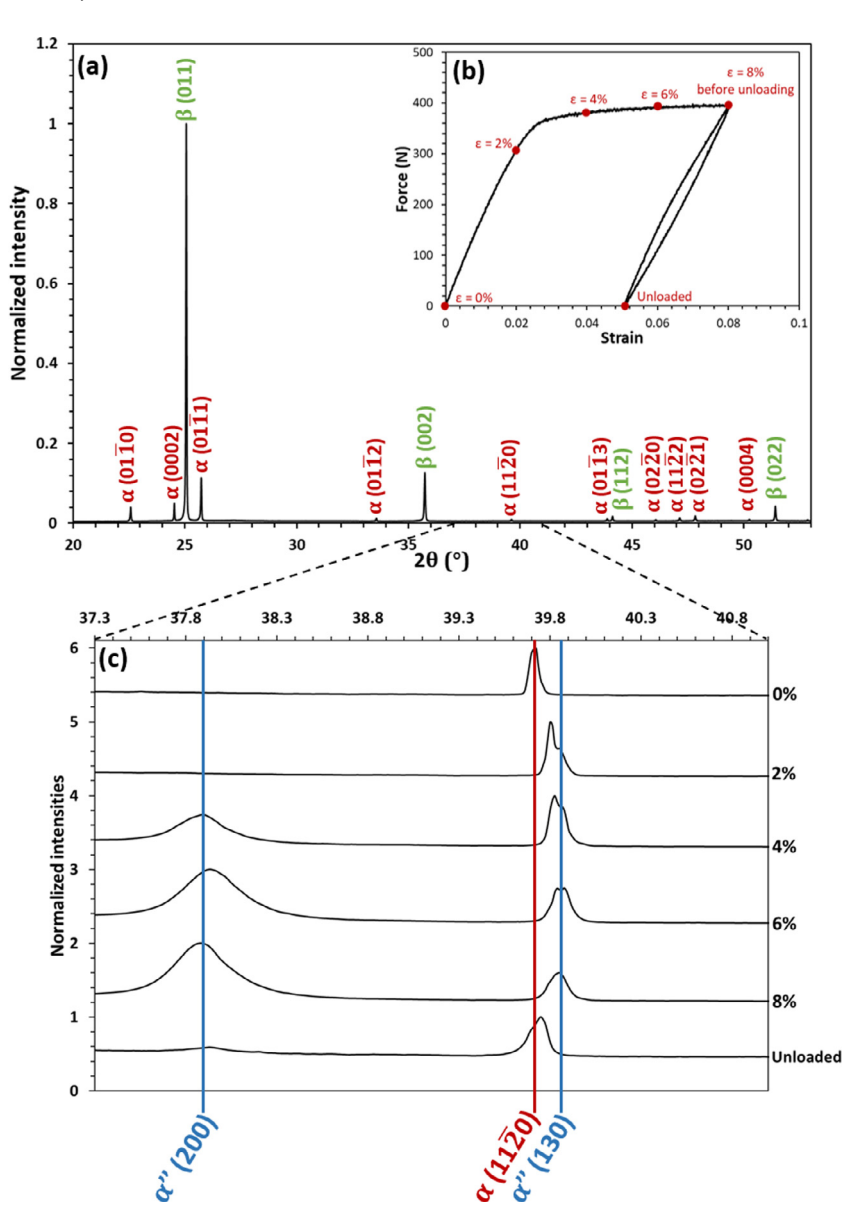


**Fig. 3.** (a) XRD at the initial state, (b) tensile test curve of the in-situ SXRD test and (c) SXRD diagrams from  $37.3^{\circ}$  to  $41^{\circ}$  of the alloy deformed from 0% to 8% and after unloading from 8%. Peaks are labeled in green for the  $\beta$  phase, in red for the  $\alpha$  phase and in blue for the  $\alpha''$  phase.

In order to further analyze these observations, the elastic strain evolution of  $\alpha$  and  $\alpha$ " peaks between 0% and 7,5% of deformation, calculated using the formula [22] are presented on Fig. 4:

$$\varepsilon_{hkl} = \frac{d_{hkl} - d_{0,hkl}}{d_{0,hkl}} \tag{1}$$

The elastic strain of the  $(11-20)\alpha$  is calculated using the position of the initial state as reference. The elastic strain of the  $(200)\alpha''$  peak is calculated using the position of peak at 2% of deformation, corresponding to the first stage where  $(200)\alpha''$  peak can be detected.

The absence of  $\beta$  peaks in the angular range limits the complete study of elastic strain partitioning between all the phases, however, it can be seen that the  $(11-20)\alpha$  and  $(200)\alpha''$  elastic strain evolutions are clearly related. It can be observed from the Fig. 4 that, at early strain, the  $(11-20)_{\alpha}$  shift is strong and almost linear, which is consistent with a marked elastic deformation and with the hypothesis that  $\alpha$  can be considered as the "hard" phase taking a lot of load, in the dual phase alloy (which correspond to the "classical" hypothesis in a  $\alpha + \beta$  microstructure). The interesting point is that, as soon as the stress-induced  $\alpha''$  martensite is observed, a sudden change of behavior of  $\alpha$  phase is actually observed

in parallel. The hypothesis would be here that the  $\alpha$  phase plastifies and progressively shed load. Meanwhile, the evolution of the  $\alpha''$  (11–20) lattice strain evolves strongly and almost linearly, suggesting that the martensite take the load on the analyzed deformation range. Consistently, a peak broadening can be observed on the (11–20) $_{\alpha}$  peak after unloading from 8% strain, suggesting that the  $\alpha$  phase is no longer an elastic inclusion at this strain level. However, the behavior of the  $\alpha$  phase has to be considered cautiously since, in the plastic regime, there is a strong interaction of the  $\alpha_p$  particles with the propagated mechanical twins which can induce additional plastic deformation by shearing.

Further detailed investigation of the deformation mechanisms has been carried out via in-situ mechanical testing in an SEM coupled with EBSD analyses. Samples have been loaded up to 5% and subsequently unloaded to 0%. The EBSD follow-up has been recorded for two different zones on the dual-phase  $(\beta+\alpha_{\rm p})$  microstructure and is presented in Fig. 5. Some of the dark zones near  $\alpha_{\rm p}$  nodules are related to a "shadow" effect. The electropolishing of the sample surface generates some roughness that hinders proper EBSD mapping in these zones. However, the EBSD analyses are able to image perfectly the strain-induced  $\alpha''$  precipitation on the 5% deformed sample, whatever the texture of the

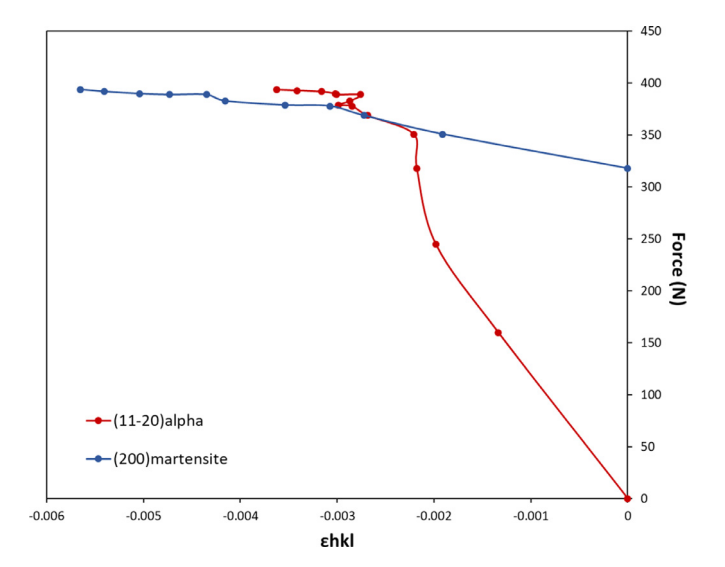


**Fig. 4.** Evolution of the elastic strain of  $(11-20)\alpha$  and  $(200)\alpha$ " peaks as a function of the force, calculated from the synchrotron XRD patterns of the alloy deformed from 0% to 7.5%, with 0.5% steps.

considered zone. One noticeable fact relates to the spatial location of the strain-induced  $\alpha''$  martensite plates in the dual-phase microstructure: every observed strain-induced  $\alpha''$  plate is observed on or close to the  $\alpha_{\rm D}/\beta$  interfaces. It raises questions regarding the origin of this straininduced product which could possibly be induced to accommodate the "mechanical contrast" between the HCP  $\alpha$  phase and the BCC  $\beta$  phase. This fact is strongly corroborated by the Schmid factor calculation associated with  $\alpha''$  precipitation in the considered zones, which are shown to be low with respect to the external (applied) stress. For example, in zone A (Fig. 5), the Schmid factor (calculated with respect to the  $\alpha''/\beta$ habit plane) with respect to the externally applied stress is comprised in the [0.2–0.3] range, suggesting that the  $\alpha''$  phase created during deformation may accommodate rather internal stresses than applied stress. This statement could additionally explain the noticeable absence of any superelastic effect associated with unloading. The present hypothesis is that the mechanisms involved here differs somehow from the "direct" TRIP effect (triggered by applied stress), commonly signed by a plateau on the stress-strain curves (absent in the present case), and followed by a bump in the stress-hardening curve. Therefore, accommodation of internal stresses may appear as an additional driving force for  $\alpha''$  martensite in dual-phase alloys. The other interesting statement is that, even if the "driving force" for stress-induced  $\alpha''$  precipitation seems mainly to be initially related to a "relaxation" process, it is reasonable to think from Fig. 4 that  $\alpha''$  play a role as an elastic inclusion. From this point, it can be therefore postulated that this may provide a notable contribution to the observed macroscopic strain-hardening. A reasonable comparison can be established with the "classical" single phase TRIP/TWIP alloys displaying a strong "bump" following the  $\alpha$ " precipitation. This bump can be interpreted as the elastic deformation contribution of the formed martensite to the overall strain-hardening, which ends when the martensite itself enters into plasticity. Additional information is also available from EBSD data (Fig. 5(a)) since large deformation bands (red arrows in zone A) are clearly displayed on 5% deformed samples. These bands can be indexed as {332} (113) deformation twins from misorientation analysis (showing a misorientation of 50.5° through the twin/matrix interface). These bands appear, however, as strongly distorted, probably because of the size of the  $\beta$  sub-grains which are observed to be of the same order of magnitude as twin length. As a result, this crystallographic distortion leads to some challenges for accurate indexing of these deformation twins. Fig. 5(a) in zone A shows some cases of interactions between {332}  $\langle 113 \rangle$  deformation twins and  $\alpha_p$  nodules, resulting in

formation of shear bands within these nodules (black arrow). Besides, this is the sign that  $\alpha_p$  nodules may actually act as strong barriers against twin propagation since some twins are stopped at the  $\alpha_p/\beta$  interfaces whereas some of these deformation twins appear to be stopped "at some distance" from these  $\alpha_p/\beta$  interfaces which could involve an additional influence of internal strain-fields or back-stresses on twin propagation. As stated earlier in this paper, the  $\alpha_p$  particles do not respect perfectly the classical BOR because they tend to form at the boundaries between misoriented  $\beta$  sub-grains during the forging sequence. This misorientation from classical BOR may induce additional internal strain-fields, on loading, strongly interacting with the deformation twins. Consequently, easy shear of  $\alpha_p$  nodules is not expected in that kind of microstructure.

The EBSD observations of the unloaded states (Fig. 5(b)) show that, consistent with the synchrotron data, the strain-induced  $\alpha''$  martensite is nearly fully reversed into the  $\beta$  phase, with very few residual  $\alpha''$  plates remaining in the unloaded microstructure. In contrast, none of the {332}  $\langle 113 \rangle$  twinning bands are reversed. An additional EBSD observation has been performed on a fractured sample near the fracture surface (see in supplementary materials, Fig. 1). It shows that a high quantity of deformation bands is visible in the  $\beta$ -matrix, leading to a very low quality of indexation (supplementary materials Fig. 1(c)), but no martensite bands are observed. It can be concluded that the residual bands are {332}<113> twins and that even at a high strain, the  $\alpha''$  phase displays a strong tendency to reverse into the  $\beta$  phase. At this stage, the complete reversion of the  $\alpha''$  phase, even at fracture stage, is not fully understood.

Based on these initial observations it can be concluded that TRIP and TWIP effects are present in Ti-1023 alloy with the dual-phase microstructure, validating the design strategy.

### 3.4. TEM investigation of {332}<113> deformation twins and their interaction with $\alpha_{\rm p}$ particles

Further detailed investigation of the highly distorted {332} (113) bands was carried out on post-deformed samples (5%) using transmission electron microscopy. Fig. 6 shows a {332} (113) deformation twin in the  $\beta$  matrix away from  $\alpha_{\rm p}$  nodules. The bright field image of the observed twin (of about 150 nm in thickness) exhibits a perfect [3-3-2]  $\langle 1-13 \rangle$  relationship with the  $\beta$  matrix (Fig. 6(a)). The band/matrix trace is parallel to the twinning interface, determined by the selected area diffraction along the 110  $\beta$  zone axis (inset of Fig. 6(a)). The observed morphology, imaged via dark field (Fig. 6(b)), is very similar to those previously observed in single  $\beta$  phase alloys, such as Ti–Mo or Ti– Cr based alloys [1],[2]. The nano-beam electron diffraction performed inside the band (inset of Fig. 6(b)) confirms that neither  $\alpha''$  precipitation, nor internal twinning take place inside the primary twin after 5% straining. However, a thin layer of  $\alpha''$  martensite, with BOR with respect to the  $\beta$  matrix, can be identified at the twin/matrix interface (Fig. 6(c) and inset). Along with the  $\alpha''$  martensite in relation with the  $\alpha_p/\beta$ , this localized martensite may be potentially induced upon loading or unloading to accommodate the strain-misfit at the twin/matrix interfaces [23]. This indicates that in the present case the  $\alpha''$  martensite is likely to be acting mainly as a local stress relaxation mechanism at the interfaces rather than a primary deformation mechanism such as deformation

When observing the {332}<113> twin in the vicinity of  $\alpha_p$  nodules, twins are observed to be highly perturbed both from the crystallographic and morphological points of view, as already observed in the EBSD maps (Fig. 5). Fig. 7 shows a deformation twin splitting into two individual branches (twinning bands) at some distance from the  $\alpha_p/\beta$  interface, probably when encountering the elastic strainfield generated from the  $\alpha_p/\beta$  elastic mismatch. Even before splitting, the {332}<113> incident twin (propagating from the left side) undergoes a crystallographic twist around the  $[1-12]_\beta$  direction. Similar phenomenon has been observed near the intersection zone of two {332}<113> twins [24]. As an illustration, two different selected area

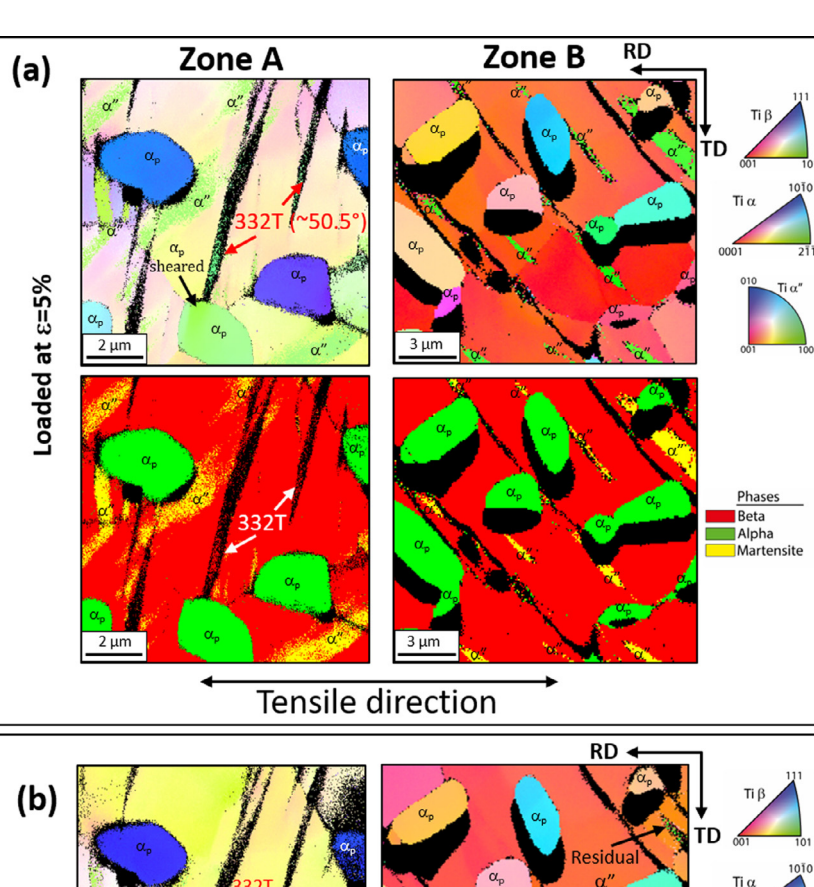
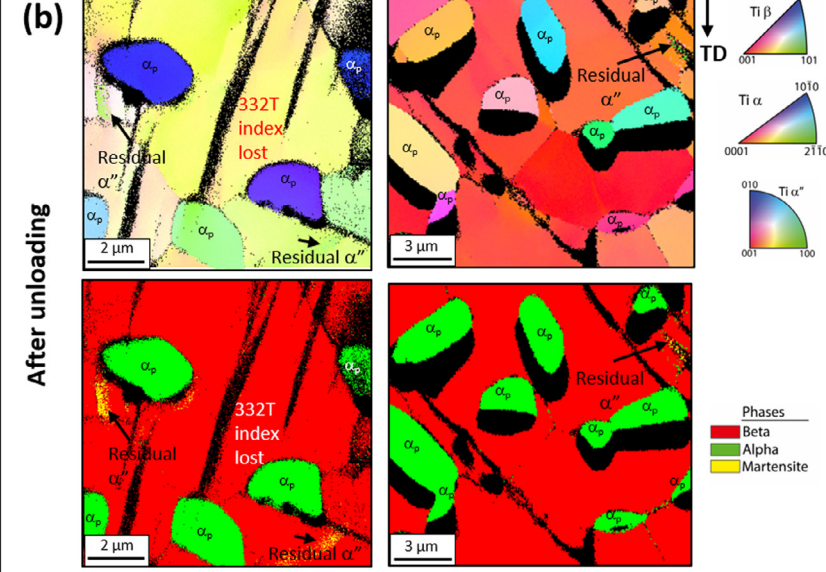


**Fig. 5.** *In-situ* follow-up of the deformation mechanisms by EBSD mapping. Normal direction Inverse Pole Figure (IPF) maps and corresponding phases maps (a) at 5% of deformation and (b) after unloading.



electron diffraction patterns (SEAD) have been recorded on the  $\beta$  matrix side (SA1) and inside the band (SA2), respectively (Fig. 7). The 332 planes are still parallel in the twisted band and the matrix, confirming the signature of 332 twinning relationship. However, when tilting along [1–12]  $\beta$  axis (black arrow in Fig. 7), almost perpendicular to the interface trace of the band, a high misorientation ( $\sim$  21°) can be measured between the two  $\langle 110 \rangle$  zone axes. This suggests a strong interaction between the incident {332}<113> deformation twin and the complex elastic strain-field in the vicinity of the  $\alpha_{\rm p}/\beta$  distorted interface.

Besides, instead of directly shearing the  $\alpha_{\rm p}$  nodule, there is a change in the twinning plane observed towards a (1–12)  $\beta$  twinning plane for a portion of the original band, resulting in a final  $\{112\}\ \langle 111\rangle$  twin from the original  $\{332\}\ \langle 113\rangle$  twin. This part of the initial twin constitutes one of the two branches, which has clearly deviated from the  $\alpha_{\rm p}$  nodule

lying on the original trajectory, after splitting. The observed  $\alpha_p$  nodule interacts with the remaining {332}  $\langle 113 \rangle$  branch of the incident deformation twin and is observed to cross the entire nodule, leaving behind a shear band. Internal misorientations have been noticed on TEM images, inside the  $\alpha_p$  nodule. Additionally, this particle shear band formation is also visible in the EBSD results from orientation gradients in several  $\alpha_p$  nodules (Fig. 5 in zone A).

It is worth noting that a noticeable residual volume fraction of  $\alpha''$  martensite can be observed inside the different twins as fine-scaled substructures as seen on the associated dark-field image (Fig. 8). This observation was absent from "isolated" twins, far from any  $\alpha_p$  particle (see Fig. 6). Therefore, it may show that  $\alpha''$  martensite is able to play a major additional role in the accommodation of internal stresses resulting from the strong elastic interactions of propagating deformation twins and  $\alpha_p$  nodules.

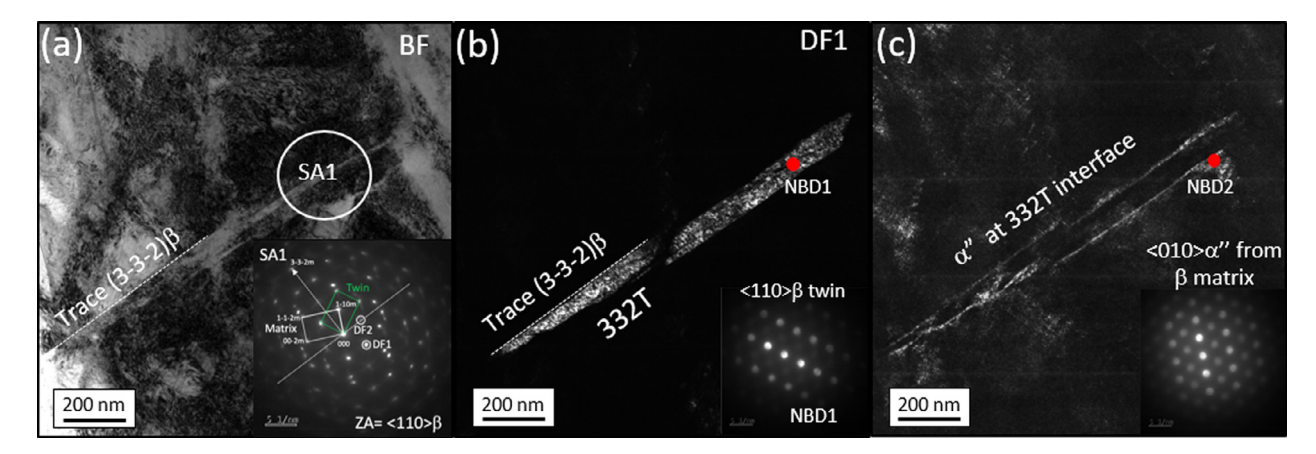


Fig. 6. TEM observations of the post-mortem sample after tensile test at  $\varepsilon$ =0.05: (a) bright field image of a {332}<113> band; (b) dark field image of the 332T band with nano beam diffraction pattern (NBD1), (c)  $\alpha''$  martensite at the 332T/matrix interface.

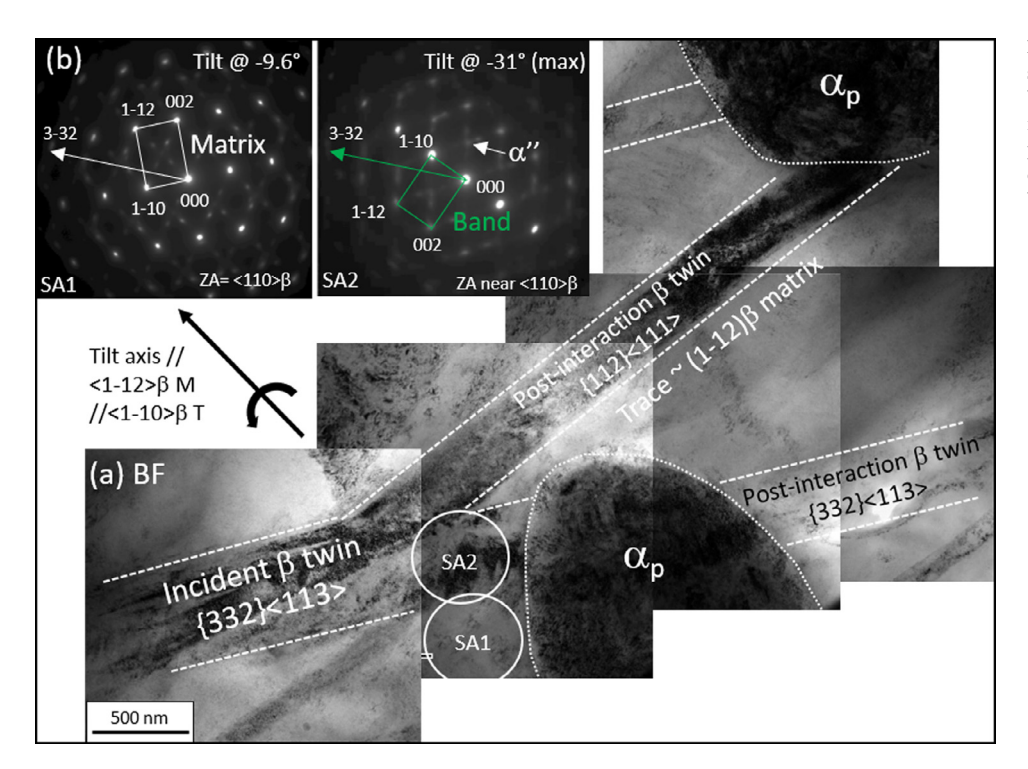
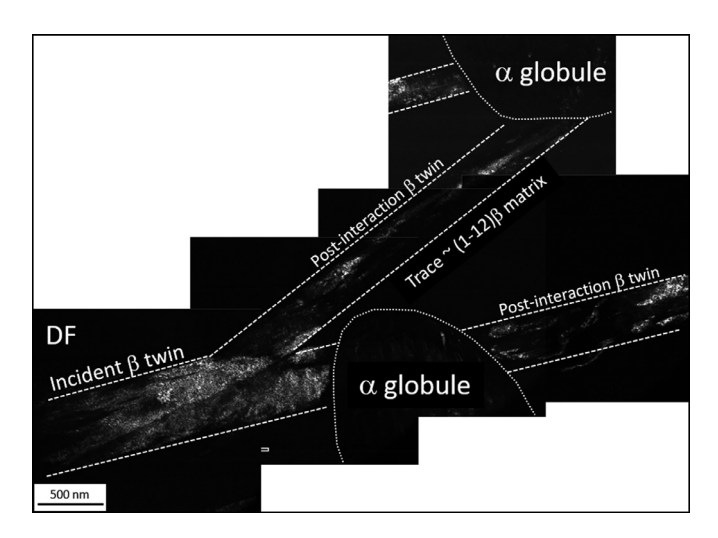


Fig. 7. TEM observations of the post-mortem sample after tensile deformation at  $\epsilon$ =0.05: (a) bright field image of a set of deformation bands interacting with a  $\alpha_p$  particle (b) diffraction patterns showing the phase constitution and orientation relationships (OR by tilting) of the band and the matrix respectively.

Bringing together all these observations leads to two sets of new insights on the deformation behavior of this dual-phase Ti-10V-2Fe-3Al forged alloy: (1) the interaction between the {332}  $\langle 113 \rangle$  mechanical twins and the primary  $\alpha_{\rm p}$  nodules is strong and complex. The nodules develop shear bands due to the direct interaction, but the experimental results clearly show strong additional elastic interactions in the vicinity of the  $\alpha_{\rm p}/\beta$  interfaces. This is rather consistent with SXRD data showing, in addition to strain-induced martensitic transformation, that the  $\alpha$ phase is strongly elastically deformed during loading, resulting in large peaks shifts (Fig. 3(c)). This should suggest a large strain-partitioning between  $\alpha$  and  $\beta$  phases, due to mechanical contrast between the two phases (generating deformation incompatibilities), and resulting in a large internal stress (back stress), growing with strain. As a consequence, stress-induced {332} (113) deformation twins are strongly interacting with the complex elastic strain fields arising due to the  $\alpha_p/\beta$  interfaces. This results in a high strain-hardening rate as displayed in Fig. 2. (2) The particular role of strain-induced  $\alpha''$  martensite is highlighted in this work. Based on the experimental results, this role is presumably not

directly associated with the accommodation of the external stress, as previously reported in case of many systems. The present results indicate that the "strain-induced"  $\alpha''$  precipitation is rather related to the relaxation of the internal stress (back-stress) as previously stated in this article. This fact is corroborated by: (a)  $\alpha''$  precipitation in the vicinity or on the  $\alpha_{\rm p}/\beta$  interfaces with an associated small Schmid factor with respect to the external stress (Fig. 5). (b)  $\alpha''$  precipitation at twin/matrix interfaces after unloading, to accommodate coherency strain between {332}  $\langle 113 \rangle$  deformation twins and  $\beta$  matrix. (c)  $\alpha''$  precipitation inside the deformation twins, following strong interactions with either  $\alpha_{\rm D}$ nodules or associated surrounding elastic strain-fields, to accommodate local distortions. These observations may show that the  $\alpha''$  precipitation in dual phase Ti-10V-2Fe-3Al is generated from heterogeneous deformation inside the microstructure rather than directly from the applied external stress. By simple analogy, the  $\alpha''$  precipitation in this case appears to play a "similar role" to the one of Geometrically Necessary Dislocations (GND) in many other heterogeneous systems: accommodation of deformation incompatibilities in the microstructure.



**Fig. 8.** TEM observations of the post-mortem sample after tensile deformation at  $\epsilon$ =0.05: dark field image of the martensite in bands interacting with a  $\alpha_p$  particle.

#### 4. Conclusions

Summarizing, it can be postulated that the extremely promising mechanical properties observed in the dual-phase Ti-10V-2Fe-3Al forged alloy result from the combined effects of: an efficient strain-hardening mechanism, directly related to both twinning propagation (dynamical Hall-Petch effect) and the additional strong twin interactions with nodular  $\alpha_n$  particles, and an efficient relaxation mechanism through  $\alpha''$ martensitic precipitation, to accommodate the different local stress concentration zones (interfaces and interactions zones). This effect probably prevents early fracture despite the heterogeneous nature of the plastic deformation. Additionally, it is reasonable to think that  $\alpha''$  play a role as an elastic inclusion: from the observation of the almost full reversibility of the  $\alpha''$  stress-induced martensite, it can be suggested that the proper deformation of this phase may be mainly elastic. As a consequence, this may provide a notable additional contribution to the observed macroscopic strain-hardening. Both effects, when combined, results in a "dynamic balance" which finally allows both high strength and high ductility with an extremely stable strain-hardening rate. Based on these results, the overall strategy developed in this work could possibly be extended to other metastable  $\beta$  titanium alloys.

#### **Declaration of Competing Interest**

The authors declare that they have no known competing financial interests or personal relationships that could have appeared to influence the work reported in this paper.

#### Acknowledgments

This work was supported by French National Agency for Research (ANR) in the ANR-15-CE08-0013 TITWIP project. YD and FP are grateful to SAFRAN company for their financial support on the YD Ph.D. grant.

#### Supplementary materials

Supplementary material associated with this article can be found, in the online version, at doi:10.1016/j.mtla.2019.100507.

#### References

F. Sun, J.Y. Zhang, M. Marteleur, T. Gloriant, P. Vermaut, D. Laillé, P. Castany,
 C. Curfs, P.J. Jacques, F. Prima, Investigation of early stage deformation mecha-

- nisms in a metastable  $\beta$  titanium alloy showing combined twinning-induced plasticity and transformation-induced plasticity effects, Acta Mater. 61 (2013) 6406–6417, doi:10.1016/j.actamat.2013.07.019.
- [2] C. Brozek, F. Sun, P. Vermaut, Y. Millet, A. Lenain, D. Embury, P.J. Jacques, F. Prima, A β-titanium alloy with extra high strain-hardening rate: design and mechanical properties, Scr. Mater. 114 (2016) 60–64, doi:10.1016/j.scriptamat.2015.11.020.
- [3] M. Marteleur, F. Sun, T. Gloriant, P. Vermaut, P.J. Jacques, F. Prima, On the design of new β-metastable titanium alloys with improved work hardening rate thanks to simultaneous TRIP and TWIP effects, Scr. Mater. 66 (2012) 749–752, doi:10.1016/j.scriptamat.2012.01.049.
- [4] S. Sadeghpour, S.M. Abbasi, M. Morakabati, A. Kisko, L.P. Karjalainen, D.A. Porter, A new multi-element beta titanium alloy with a high yield strength exhibiting transformation and twinning induced plasticity effects, Scr. Mater. 145 (2018) 104–108, doi:10.1016/j.scriptamat.2017.10.017.
- [5] L. Lilensten, Y. Danard, C. Brozek, S. Mantri, P. Castany, T. Gloriant, P. Vermaut, F. Sun, R. Banerjee, F. Prima, On the heterogeneous nature of deformation in a straintransformable beta metastable Ti-V-Cr-Al alloy, Acta Mater. 162 (2019) 268–276, doi:10.1016/j.actamat.2018.10.003.
- [6] J. Gao, Y. Huang, D. Guan, A.J. Knowles, L. Ma, D. Dye, W.M. Rainforth, Deformation mechanisms in a metastable beta titanium twinning induced plasticity alloy with high yield strength and high strain hardening rate, Acta Mater. 152 (2018) 301– 314, doi:10.1016/j.actamat.2018.04.035.
- [7] L. Ren, W. Xiao, C. Ma, R. Zheng, L. Zhou, Development of a high strength and high ductility near β-Ti alloy with twinning induced plasticity effect, Scr. Mater. 156 (2018) 47–50, doi:10.1016/j.scriptamat.2018.07.012.
- [8] M. Abdel-Hady, K. Hinoshita, M. Morinaga, General approach to phase stability and elastic properties of β-type Ti-alloys using electronic parameters, Scr. Mater. 55 (2006) 477–480, doi:10.1016/j.scriptamat.2006.04.022.
- [9] F. Sun, J.Y. Zhang, P. Vermaut, D. Choudhuri, T. Alam, S.A. Mantri, P. Svec, T. Gloriant, P.J. Jacques, R. Banerjee, F. Prima, Strengthening strategy for a ductile metastable β-titanium alloy using low-temperature aging, Mater. Res. Lett. 5 (2017) 547–553, doi:10.1080/21663831.2017.1350211.
- [10] M. Ahmed, D. Wexler, G. Casillas, O.M. Ivasishin, E.V. Pereloma, The influence of β phase stability on deformation mode and compressive mechanical properties of Ti–10V–3Fe–3Al alloy, Acta Mater. 84 (2015) 124–135, doi:10.1016/j.actamat.2014.10.043.
- [11] X. Ma, F. Li, J. Cao, J. Li, Z. Sun, G. Zhu, S. Zhou, Strain rate effects on tensile deformation behaviors of Ti-10V-2Fe-3Al alloy undergoing stress-induced martensitic transformation, Mater. Sci. Eng.: A 710 (2018) 1–9, doi:10.1016/j.msea.2017.10.057.
- [12] C. Li, X. Wu, J.H. Chen, S. van der Zwaag, Influence of α morphology and volume fraction on the stress-induced martensitic transformation in Ti–10V–2Fe–3Al, Mater. Sci. Eng.: A 528 (2011) 5854–5860, doi:10.1016/j.msea.2011.03.107.
- [13] L. Qi, X. Qiao, L. Huang, X. Huang, X. Zhao, Effect of structural stability on the stress induced martensitic transformation in Ti–10V–2Fe–3Al alloy, Mater. Sci. Eng.: A 756 (2019) 381–388, doi:10.1016/j.msea.2019.04.058.
- [14] C. Li, J. Chen, W. Li, J.J. He, W. Qiu, Y.J. Ren, J.L. Chen, J.H. Chen, Study on the relationship between microstructure and mechanical property in a metastable β titanium alloy, J. Alloys Compd. 627 (2015) 222–230, doi:10.1016/j.jallcom.2014.12.100.
- [15] C. Le Bourlot, P. Landois, S. Djaziri, P.-.O. Renault, E. Le Bourhis, P. Goudeau, M. Pinault, M. Mayne-L'Hermite, B. Bacroix, D. Faurie, O. Castelnau, P. Launois, S. Rouzière, Synchrotron X-ray diffraction experiments with a prototype hybrid pixel detector, J. Appl. Cryst. 45 (2012) 38–47, doi:10.1107/S0021889811049107.
- [16] S. Basolo, J.F. Bérar, N. Boudet, P. Breugnon, B. Chantepie, J.C. Clémens, P. Delpierre, B. Dinkespiler, S. Hustache, K. Medjoubi, M. Ménouni, C. Morel, P. Pangaud, E. Vigeolas, A 20kpixels CDTE photon-counting imager using XPAD chip, nuclear instruments and methods in physics research section A: accelerators, spectrometers, Detect. Assoc. Equip. 589 (2008) 268–274, doi:10.1016/j.nima.2008.02.042.
- [17] W. Wang, X. Zhang, J. Sun, Phase stability and tensile behavior of metastable β Ti-V-Fe and Ti-V-Fe-Al alloys, Mater. Charact. 142 (2018) 398–405, doi:10.1016/j.matchar.2018.06.008.
- [18] Q. Xue, Y.J. Ma, J.F. Lei, R. Yang, C. Wang, Mechanical properties and deformation mechanisms of Ti–3Al–5Mo–4.5V alloy with varied β phase stability, J. Mater. Sci. Technol. (2018), doi:10.1016/j.jmst.2018.04.004.
- [19] I. Gutierrez-Urrutia, C.-L. Li, S. Emura, X. Min, K. Tsuchiya, Study of (332)<113>twinning in a multilayered Ti-10Mo-xFe (x=1-3) alloy by ECCI and EBSD, Sci. Technol. Adv. Mater. 17 (2016) 220–228, doi:10.1080/14686996.2016.1177439.
- [20] J.Y. Zhang, J.S. Li, Z. Chen, Q.K. Meng, F. Sun, B.L. Shen, Microstructural evolution of a ductile metastable β titanium alloy with combined TRIP/TWIP effects, J. Alloys Compd. 699 (2017) 775–782, doi:10.1016/j.jallcom.2016.12.394.
- [21] F. Sun, Y.L. Hao, S. Nowak, T. Gloriant, P. Laheurte, F. Prima, A thermo-mechanical treatment to improve the superelastic performances of biomedical Ti–26Nb and Ti–20Nb–6Zr (at%) alloys, J. Mech. Behav. Biomed. Mater. 4 (2011) 1864–1872, doi:10.1016/i.imbbm.2011.06.003.
- [22] H. Van Swygenhoven, S. Van Petegem, In-situ mechanical testing during X-ray diffraction, Mater. Charact. 78 (2013) 47–59, doi:10.1016/j.matchar.2012.12.010.
- [23] S.A. Mantri, F. Sun, D. Choudhuri, T. Alam, B. Gwalani, F. Prima, R. Banerjee, Deformation induced hierarchical twinning coupled with omega transformation in a metastable β-Ti alloy, Sci. Rep. 9 (2019) 1334. doi:10.1038/s41598-018-37865-0.
- [24] J. Zhang, F. Sun, Z. Chen, Y. Yang, B. Shen, J. Li, F. Prima, Strong and ductile beta Ti–18Zr–13Mo alloy with multimodal twinning, Mater. Res. Lett. 7 (2019) 251–257, doi:10.1080/21663831.2019.1595763.